

Electrohydrodynamically Assisted Deposition of Efficient Perovskite Photovoltaics

Hidetaka Ishihara, Wenjun Chen, Yen-Chang Chen, Som Sarang, Nicholas De Marco, Oliver Lin, Sayantani Ghosh, and Vincent Tung*

Organic–inorganic perovskites that combine the strength of both chemical worlds have emerged as tantalizing candidates for next generation photovoltaics. Here, the electrohydrodynamically assisted continuous liquid interface propagation as a general, and potentially scalable nanomanufacturing route toward synthesizing high quality perovskite thin films in a rapid and high throughput fashion is reported. This strategy conceptually mimics the advantageous self-organizing features of emulsion droplets where the use of a binary solvent system, concurrently and continuously, initiates a three-stage process of coalescence, spreading, and merging, thus optimizing thin film morphology upon deposition without the needs for additional engineering steps. The resulting perovskite thin film not only exhibits a smooth topology with the root mean square roughness of only a few nm but also reveals hybrid morphology where micrometer-sized grains intersperse between interconnected and continuous crystalline networks. This gives rise to the highest power conversion efficiency of 16.50% and average 14.68%; representing a nearly twofold increase compared to that of conventional spray-pyrolysis approach. As a final critical aspect, the proposed strategy contributes new insights to efficiently managing the environmentally hazardous lead during processing, significantly reducing the amount by two orders of magnitude compared to that of spin-coating to achieve the same thin film thickness.

1. Introduction

Over the past five years, rapid advancement in organic–inorganic perovskites has fascinated scientists across different disciplines because of their appropriate direct bandgap,^[1] high absorption coefficient,^[2] low processing temperature,^[3] exceptional carrier transport,^[4] ease of bandgap engineering,^[5] long-range carrier lifetime,^[6] and most importantly, the potential to achieve grid competitive efficiency over 20%^[7,8] at a low manufacturing budget.^[1,6,9,10] In particular, the convergence of exceptionally superior output characteristics, low processing

temperature, and solution processability makes it possible for the realization of a high throughput, roll-to-roll production process of high efficiency photovoltaics, thus ending the gap between academic prototypes and industrial standards. While the prospect of harnessing these advantageous properties makes perovskites ideal candidates for next generation solar cells, there are roadblocks hindering widespread deployment. Two of the major challenges are: (a) the lack of a proper processing route that is compatible with in-line production while generating thin films with both the material quality and morphology required to effectively harness solar irradiation and extraction of charge carriers at interfaces and (b) efficient management of the environmentally toxic element, e.g., lead (Pb).

Thus far, spin-coating represents one of the most widely employed production routes in solution processed perovskite photovoltaics. Convective flow during spinning and the subsequent evaporation process induce rapid and strong ionic interactions between metal cations and organic anions, leading to the formation of well-crystallized structure. However, the overall morphology is neither homogenous nor continuous over the entire functional area unless lengthy thermal annealing,^[11] sequential deposition,^[12] multistep solvent infiltration at interfaces,^[13] post solvent engineering,^[14,15] or hot casting^[16] are implemented. The need for additional processing steps adversely interrupts the fabrication process and creates extra manufacturing complication and cost in scaling up. Further, excessive amounts of perovskite precursor solutions are wasted as a result of centrifugal forces, thus generating unwanted Pb wastes. Built upon the successful demonstration of printable polymer photovoltaics,^[17] spray coating techniques have been revisited to circumvent these formidable challenges as they potentially enable a glass-in-module-out processing technique for cost-effective and scalable production of large-area photovoltaics (the amount of solute directly scales with the volume of the precursor solutions deposited on the substrates). In essence, fine droplets containing perovskite precursors with a polydispersed distribution of diameters are iteratively deposited onto the substrates until a desired thickness is achieved.^[18,19] When incoming droplets meet the surface at a non-zero contact angle, the contact line is pinned to its initial

Dr. H. Ishihara, W. Chen, Y.-C. Chen,
N. De Marco, O. Lin, Prof. V. Tung
School of Engineering
University of California
Merced, CA 95343, USA
E-mail: vtung@lbl.gov
S. Sarang, Prof. S. Ghosh
School of Nature Science
University of California
Merced, CA 95343, USA



DOI: 10.1002/admi.201500762

position (Figure S1a, Supporting Information). This geometrical constraint limits the interaction between adjacent droplets, preventing coalescing, spreading, and ultimately merging into a uniform thin film. Instead, de-wetting of individual droplets dominates and therefore results in radial, spoke-like patterns of perovskite crystals that not only comprise of a high density of intra- and intergranular defects but also show extremely rough morphology with peak-to-valley variation of up to a few tenths of micrometers.^[19,20] As a result, the overall photovoltaic characteristics still fall short of those made by thermal evaporation and spin-casting counterparts because of the defect-plagued morphology (Figure S1b, Supporting Information). It is known that the absorption profile and carrier transport of perovskite photovoltaics are highly dependent on the crystallinity, uniformity, and integrity of the perovskite thin film.^[21] Furthermore, unlike soft polymeric absorbers with dynamic self-organizing capabilities, the morphological optimization of spray-coated perovskite will have to be completed at the deposition stage before unwanted drying and irreversible crystallization take place at a relatively low transition temperature (≤ 100 °C). In light of this, research directed at understanding how to regulate the deposition of incoming perovskite droplets, i.e., whether a droplet undergoes coalescing, spreading, drying, or de-wetting, is central to the potential for high throughput production of high quality perovskite thin films. This would also hold great promise for reducing the reliance on environmentally toxic Pb through an efficient management during deposition.

Recent advances in understanding hydrodynamics of liquid droplets suggest that the morphology of the thin film deposition is greatly influenced by their local microenvironment through a combination of geometric and physical cues. To date, geometric stimuli in the form of nanostructured texture, and surface tension engineering are the most prevalent and best-characterized approaches. In contrast, relatively little is explored regarding physical routes for directing hydrodynamics of impacting droplets. Understanding the accompanying physical phenomena will permit the direct manipulation of thin film characteristics including coverage, uniformity, thickness, grain sizes, and low grain-boundary activity, ultimately leading to a low non-radiative recombination for high power conversion efficiency (PCE). Here, we report a continuous liquid interface propagation (CLIP) of perovskites enabled by electrohydrodynamic (EHD) assembly as a potentially scalable, general, and yet versatile nanomanufacturing route to synthesize high quality perovskite thin films with desired morphology, enhanced coverage, well-defined crystallinity, and improved photovoltaic characteristics in a rapid and high throughput fashion. It takes at most ≈ 6 – 8 s (a single pass) to create a uniform coating of perovskite thin film with a tunable thickness on a 1.5 cm \times 1.5 cm substrate and the results exhibit improved uniformity comparable to that of spin-coating specimens with a peak-to-valley variation of only approximately few nm after thermal annealing. (Highest and lowest achievable thicknesses are 750 and 250 nm, respectively.) The solution-based approach allows for judicious control over thin film thickness, morphology, and uniformity and the flexibility of solution chemistry for compositionally engineered perovskites. Further, incorporating a dual-sourced CLIP approach allows for piecing together building blocks

comprised of organic and inorganic moieties without the need for common solvent characteristics. Of particular importance is that the CLIP process significantly reduces the consumption of Pb by two orders of magnitude compared to that of conventional spin-casting, thus mitigating the pressing issues of Pb contamination.

In spray-on solar cell fabrication, atomization of high densities of droplets is employed to ensure a sufficient coverage over the targeted area. From a hydrodynamic perspective, the outcome of the impacting droplets, e.g., merging into thin film or drying individually, is proportional to the product of dimensionless constant of $We^{1/2}Re^{1/4}$, where We is the droplet Weber number, $We = \frac{\rho DV_0^2}{\sigma}$ and Re is the droplet Reynolds number, $Re = \frac{\rho DV_0}{\mu}$. ρ , D , V_0 , σ , and μ denote liquid density, droplet diameter, impact velocity, surface tension, and viscosity, respectively.^[22] It is known that effective promotion of the desired deposition phenomenon requires V_0 and σ to be synergistically minimized while concurrently maximizing D .^[23] To this end, we have systematically explored several approaches and are particularly intrigued by the readily accessible EHD process (well known for its use in electrospinning and spraying), as schematically illustrated in **Figure 1a** and Scheme S1. For decades, it has been known that the EHD process can atomize liquid medium for high throughput production of thin film specimens.^[24] A high voltage applied between a nozzle and a conductive support plate creates an electrohydrodynamic phenomenon that drives the flow of colloidal dispersions out of the nozzle, which later disintegrates into highly charged droplets. Different from spray coating, where droplets randomly deposit onto the substrates, external electric fields preferentially guide these electrostatically charged droplets onto collecting area, thus significantly enhancing the yield and coverage. Next, upon the immediate contact of droplets and substrate, saturated solvent vapor at the interface creates a thin lamella film on the substrate, providing a low surface tension medium as well as forming a saturated microenvironment to reduce the impact of downward V_0 of the droplets. In addition, the thin lamella can also be deemed as a seeding layer to facilitate the coalescence of droplets into a thin film. Meanwhile, previous studies as well as our work on the rapid deposition of self-aligned, mono-layered nanocarbon allotropes, including pristine graphene and carbon nanotubes, suggested that a two-solvent system (especially two miscible solvents with different vapor pressures and similar boiling points, b.p.) significantly enhances the spreading of the deposited liquid into areas of substrates not directly covered by the spray.^[25] In other words, incoming droplets continuously coalesce upon deposition, and then dynamically spread into uniform thin films without drying individually.

2. Results

To benchmark our CLIP process, we focused on the archetypical mixed halide perovskites, $CH_3NH_3PbI_{3-x}Cl_x$, because of consistent output characteristics even when processed in ambient conditions.^[26] In a typical deposition, a precursor solution comprising methylammonium iodide (MAI) and lead chloride ($PbCl_2$) (molar ratio, 3:1; 2.64 M for MAI and 0.88 M

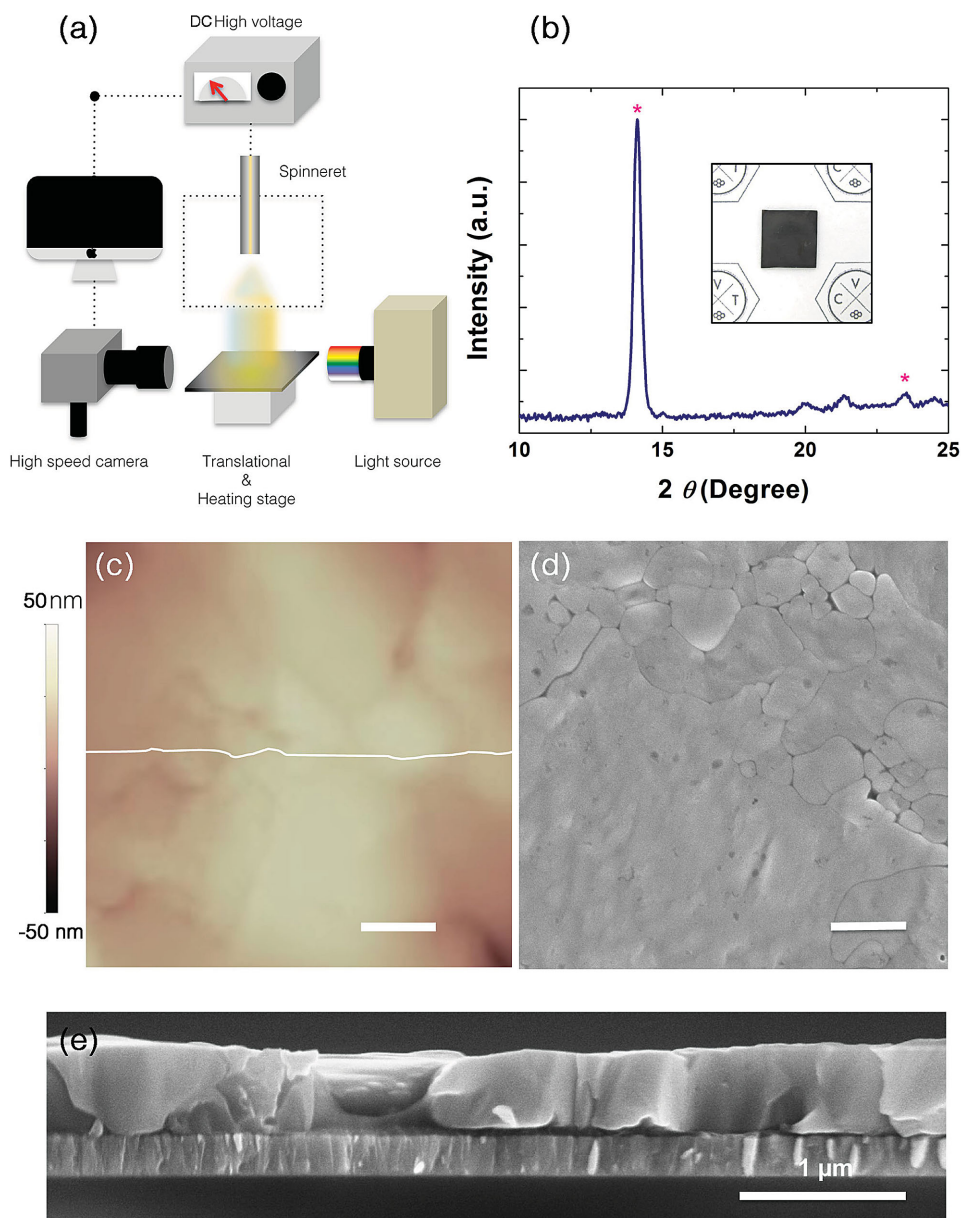
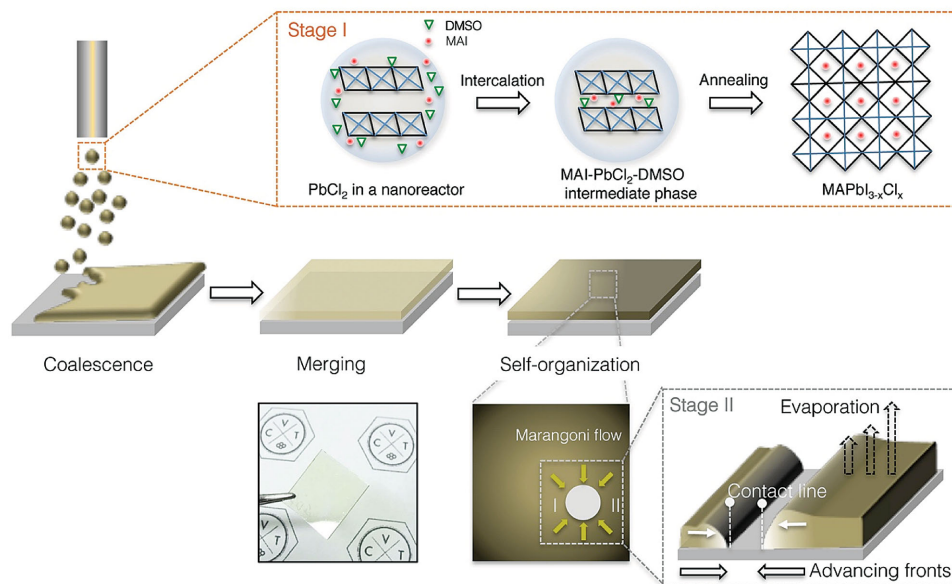


Figure 1. EHD assisted CLIP production of perovskites. a) Schematic illustration depicts the setup of the CLIP process. b) XRD, c) AFM, d) SEM, and e) corresponding cross-sectional SEM collectively show the crystallinity, uniformity, and integrity of the perovskite thin films. Inset displays the perovskite thin film deposited on an ITO substrate. The resulting thin films appear to be dark brown in color and are visibly uniform throughout the substrates. Scale bars are 2 μm in AFM and SEM.

for PbCl_2) is dissolved in a mixture of anhydrous dimethyl sulfoxide (DMSO) and *N*-methyl-2-pyrrolidione (NMP) with an optimized ratio (v/v, 4–6), followed by EHD spraying at a feed rate of $18 \mu\text{L min}^{-1}$, moving speed of the translation stage at 3.2 mm s^{-1} , and a surface temperature at $35 \text{ }^\circ\text{C}$, respectively. As schematically depicted in **Scheme 1**, a high DC voltage (kV) is applied between the nozzle tip and the metal plate using a computer controlled power supply to generate an electric field that causes charged species within the liquid medium to accumulate near the surface of the pendent meniscus. Upon reaching the threshold electric field ($\approx 5 \text{ kV cm}^{-1}$), the electrostatic stress overcomes the capillary tension at the apex of the

liquid cone, giving rise to fine, charged droplets. External electric fields electrostatically guide the charged droplets onto the substrates. Next, incoming droplets immediately coalesce on the substrate, ultimately merging into a uniform thin film as a result of much reduced surface tension (Video S1, Supporting Information). Unlike the conventional spray coating approach where droplets contract right after deposition (Video S2, Supporting Information), the resulting thin film is strikingly uniform over the entire substrate and remains yellowish and wet even after 15 min inside a petri dish. This is intriguing as most of the perovskite thin films made by spray-coating quickly turn into a hazy brown color right after deposition even if solvents



Scheme 1. Self-organization and Marangoni flow.

with high boiling points are used. Finally, the color of the perovskite thin films gradually turns into a dark brown to matte black upon a heat-gun-assisted annealing at 110 °C for 6 min as indicated in the inset of Figure 1b and Scheme S1b (Supporting Information). The X-ray diffraction (XRD) pattern confirms the highly crystalline and oriented nature of the perovskite thin film emanating from the sharp (110) and (220) peaks, respectively (Figure 1b). In parallel, the morphology of perovskite thin film fabricated by CLIP process was systematically examined through both atomic force microscopy (AFM, Figure 1c) and scanning electronic microscopy (SEM, Figure 1d), respectively. The resulting thin film not only shows a smooth topology with the root mean square roughness of only a few nm but also reveals a random distribution of micrometer-sized grains interspersed between interconnected crystalline networks. This is in a stark contrast with previous strategies, as the deposition duration of the proposed EHD spraying is remarkably short and does not involve heat-assisted flash welding of crystalline domains or the post-diffusion of secondary solvent with immiscible solubility characteristics.^[8,16]

Intuitively, one would expect that the underlying mechanism of the EHD-enabled CLIP process to greatly resemble that of polymer-blended composites, e.g., solvent vapor-induced self-organization. As suggested in temporally resolved morphological evolution, solvent evaporation gradually drives the formation of molecularly ordered and sterically interlocked stacking between polymers and fullerene additives.^[27] It is thus evident that the optimization of morphology in the polymer blended cases predominately hinges on the degree of solvent engineering. In contrast, the self-organizing feature in CLIP process occurs in a hierarchical and more prompt fashion. At a molecular level, the charged droplets provide seemingly infinite interfaces for efficient intercalation of MAI and DMSO between PbCl₂ to take place, thus forming an MAI-PbCl₂-DMSO intermediate phase similar to that previously reported (stage I, Scheme 1 and Figure S2, Supporting Information).^[14] Wet films

made of intermediate phases are known to be very uniform, flat, and self-organized in nature, forming a solid foundation for subsequent conversion into the perovskite phases with desired morphological features. At the nanoscale, the combination of two solvents with dissimilar fluid dynamic characteristics (where the two miscible liquids differ by their volatility and surface tension) tends to create preferential evaporation of the relatively volatile solvent, e.g., DMSO (DMSO, surface tension of 43.54 mN m⁻¹ at 20 °C and b.p. of 189 °C; NMP, surface tension of 40.79 mN m⁻¹ at 20 °C and b.p. of 202 °C). The locally unsaturated vapor pressure therefore drives the spreading phenomena, originating from a nano-Marangoni effect, that can be

expressed as $V_c^2(x) = \frac{1}{2\eta(x)} \frac{d\sigma}{dx} x(1-x)(-A_l\alpha_l + A_h\alpha_h)$, where

V_c is the Marangoni velocity, η is the viscosity of the film, σ is the surface tension, x is the volume fraction of the low surface tension solvent, and A is the evaporation capacity, induced by evaporation from a two-component mixture.^[27,28] Further, the formation of such dynamic solvent fronts also in turn mobilizes the initially static pinning lines to recover the un-wetted areas and pinholes (stage II, Scheme 1), paving a homogenous coverage. We thus surmise that the combination of these advantageous self-organizing features at different length scales simultaneously and continuously trigger the continuous liquid interface propagation of MAI-PbCl₂-DMSO intermediate phases upon deposition.

Indeed, morphological and topological characterizations as well as perspective views from 3D profiles collectively corroborate the proposed mechanism (Figure 2). Although perovskite droplets made of a pure DMSO microenvironment did settle and merge into thin films upon deposition due to the formation of self-organizing MAI-PbCl₂-DMSO intermediate phases, it is the lack of secondary solvent that results in the static solvent fronts and unwanted contraction. Consequently, wet perovskite thin film tends to rupture upon thermal annealing and thus exhibits inhomogeneous morphology filled with voids and

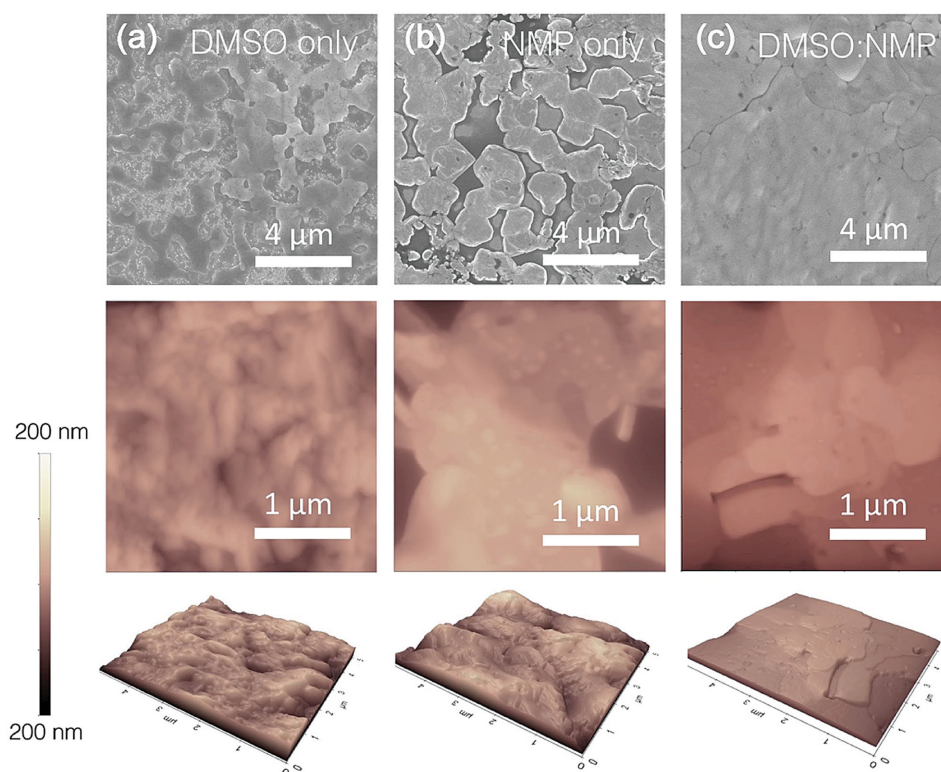


Figure 2. Morphological, topological, and 3D profile characterizations. Morphological features (top panel), topological variations (middle panel), and 3D profiles (bottom panel) of a) DMSO only, b) NMP only, and c) the combination of both solvents collectively underscore the importance of self-organizing features enabled by nano-Marangoni flows. Thin films without nano-Marangoni flow often display jagged edges and rugged terrain, adversely affecting the fidelity and efficiency of carrier transport.

rugged terrains, leading to a hill-to-valley variation up to few tenths of micrometers (Figure 2a). In the pure NMP control experiment, retraction process dominates as perovskite thin films quickly break into sessile droplets during EHD deposition, thus leaving behind a textile-like morphology with discontinuous grains and distributed craters after thermal annealing as shown in Figure 2b. The formation of these largely uneven and separated perovskite islands is problematic as the subsequent deposition of electron extraction layer, e.g., fullerene derivatives, forms a direct contact with the underlying hole transport layer, creating energetically unfavorable shunting pathways. Discrete perovskite islands gradually converged into densely packed and morphologically uniform thin films when the optimized solvent composition was reached (Figure 2c), thus underscoring the importance of multiscale self-organizing features. Detailed processing conditions can be found in the Experimental Section and Table S1 (Supporting Information), respectively.

The ability to create uniform perovskite thin films with continuous crystalline grains in all directions also greatly enhances the reproducibility, fidelity, and scalability for subsequent photovoltaic fabrication. The cross-sectional SEM images reveal more information about the crystalline size. Unlike the conventional spray-coating that typically exhibits a coin-stacked cross-section, the perovskite thin film prepared by the CLIP process displays sharp and continuous interfaces with the absence of apparent grain boundaries even when thickness exceeds 1 μm (Figure S3, Supporting Information). This translates to

the photogenerated charge carriers being able to leverage the energetically favorable, readily established transport pathways in both in-plane and out-of-plane directions within the perovskite thin films. UV-vis absorption spectra, especially the increasing band-edge absorption around 750 nm, scale well with the increased thickness of the perovskite thin films (Figure S4, Supporting Information). In parallel, the uniformity and/or the complete reaction of the perovskite precursors are also evident in the energy dispersive X-ray spectroscopy (EDX) mapping elemental analysis. We mapped out the relevant elemental distribution (Pb in blue, C in red, Cl in yellow, I in cyan, and the mixture of all three elements) with EDX in the cross-sectional SEM as shown in **Figure 3**. While the outlines of Pb, C, and I overlay very well with the corresponding cross-sectional SEM image, the Cl map only shows limited distribution throughout the entire cross section. The calculated atomic ratio of Cl/(Cl+I) is way less than 2% reported previously which is significantly lower than that of the compositional stoichiometry in the precursor solutions due to the removal of volatile byproducts, $\text{CH}_3\text{NH}_3\text{Cl}$ (MACl). While the role of Cl has not been conclusively determined, several reports have collectively pointed out the existence of Cl ions effectively promote the crystal growth in a 3D fashion to improve the crystallinity and associated charge carriers dynamics.^[29] These compelling structural and morphological features collectively make CLIP assembled perovskites well suited for using as active layers to efficiently harvest irradiant sunlight.

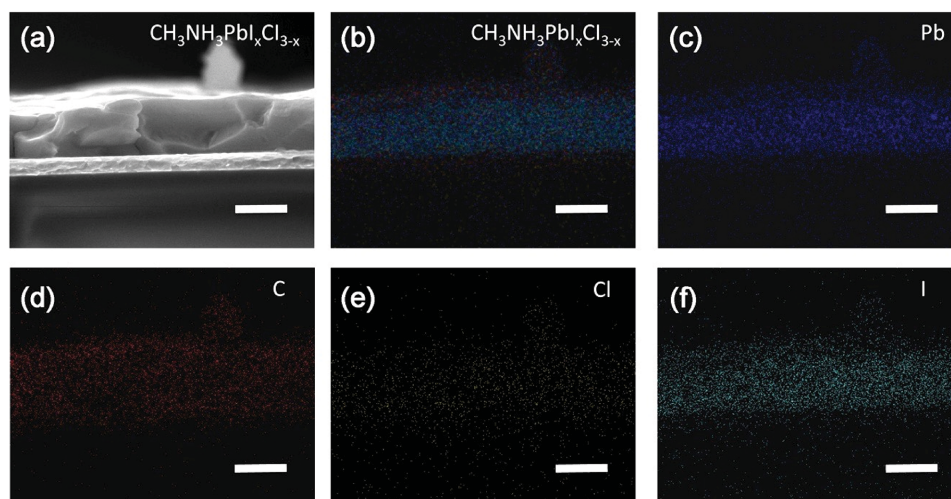


Figure 3. Spatial distribution of relevant elements within perovskite thin films. a) Cross-sectional SEM image reveals the chunky, continuous crystalline grains of perovskites. The exceedingly large grains produced by one step CLIP process establish uninterrupted pathways for dissociated carriers between cathode and anode, without encountering the energetically unfavorable traps. Corresponding EDX mapping shows the spatial distribution of relevant elements within perovskites, including b) overlaid $\text{CH}_3\text{NH}_3\text{PbI}_{3-x}\text{Cl}_x$, c) Pb in blue, d) C in red, e) Cl in yellow, and f) I in cyan, respectively. Scale bars are 500 nm.

3. PV Characteristics

To this end, a planar photovoltaic cell that comprises indium tin oxide (ITO)/poly(3,4-ethylenedioxythiophene) polystyrene sulfonate (PEDOT:PSS)/perovskites/phenyl- C_{61} -butyric acid methyl ester ($[\text{C}_{60}]\text{PCBM}$)/fullerene (C_{60})/aluminum (Al) was fabricated and systematically examined. The perovskite thin film with thickness of ≈ 600 nm was directly deposited through the EHD-assisted CLIP process (electric field of 5 kV cm^{-1} , flow rate of $18 \mu\text{L min}^{-1}$, deposition time ≈ 6 s, and surface temperature of 35°C) onto ITO substrates pre-coated with a thin hole transport layer of PEDOT:PSS (40 nm), followed by a heat gun annealing process at 110°C for 6 min (Scheme S1b, Supporting Information). Note that the uniformity of thin films can be further improved by a short UV-ozone treatment (≈ 40 s) on PEDOT:PSS prior to perovskite deposition. Next, an electron extraction layer of C_{60}PCBM (2 wt% in dichlorobenzene) was directly spin-coated at 3000 rpm onto the perovskite layer and then annealed at 100°C for an hour. Another layer of C_{60} (30 nm) is thermally evaporated to act as both an additional blocking and electron transport layer. Finally, Al electrodes were thermally evaporated to complete the device. **Figure 4a** schematically illustrates the final device architecture and the corresponding false colored, cross-sectional SEM image. Sharp and well-defined interfaces between perovskite (light gray) and neighboring transport layers with $\text{C}_{60}\text{PCBM}/\text{C}_{60}$ in magenta and PEDOT:PSS/ITO in blue are clearly distinguished. In particular, the continuous, slab-like grains extend effectively to bridge the modification layers of opposite polarities. Self-dissociated charge carriers under external electric fields can essentially propagate to the collecting electrodes without encountering energetically unfavorable traps. Indeed, average current-voltage (I - V) output characteristics from 20 devices depicted in **Figure 4b** collectively show a short circuit current (J_{sc}) of 21.07 mA cm^{-2} , an open circuit voltage (V_{oc}) of 0.97 V , and fill factor (FF) of 0.72 , thus giving rise to average

power conversion efficiency (PCE) of 14.68% under AM 1.5G. The reported PCE represents a nearly two-fold increase compared to that of conventional spray-pyrolysis approach (J_{sc} of 14.90 mA cm^{-2} , V_{oc} of 0.84 V , FF of 0.63 , and PCE of 7.88%) and is highest among all the spray-coated approaches.^[19] We occasionally observed that PCE well exceeds 16.50% but is not included in this work. Nevertheless, given the relatively simple device architecture, we envision that the output characteristics can be readily improved by the interfacial engineering and the use of double blocking layer to suppress the possible leakage current. Meanwhile, external quantum efficiency (EQE) spectrum shows an onset of photocurrent at 790 nm , a characteristic bandgap of $\text{CH}_3\text{NH}_3\text{PbI}_{3-x}\text{Cl}_x$. The EQE gradually increases in a monotonic manner and reaches a plateau at 625 nm . Specifically, the average EQE is beyond 80% at the spectral range of $450\text{--}600 \text{ nm}$. The facile and high throughput CLIP process also shows a high reproducibility as is evident in the narrow distribution of histogram of photovoltaic PCEs over 20 devices as suggested in **Figure 4d**. In addition, the utility of the versatile CLIP approach is further demonstrated by the incorporation of dual sources (**Figure S5a**, Supporting Information). This dual-sourced setup bears a close resemblance to that of vacuum evaporation where building blocks comprised of organic and inorganic moieties can be rationally pieced together without the need for common solvent characteristics. As a first proof of concept, perovskite precursors dissolved in NMP and DMSO, respectively, were sprayed from two different sources. Similar to the single sourced CLIP process, incoming droplets first quickly merge into a semi-transparent thin film but slowly turned to a yellowish color after being placed inside a petri dish for few minutes (**Figure S5b**, Supporting Information), presumably due to the relatively slow intercalation, organization, and optimization of perovskite precursors at macroscale. Aside from the prolonged diffusion process at interfaces, the resulting thin film converts into well-crystallized perovskites with comparable morphology and compositional distribution

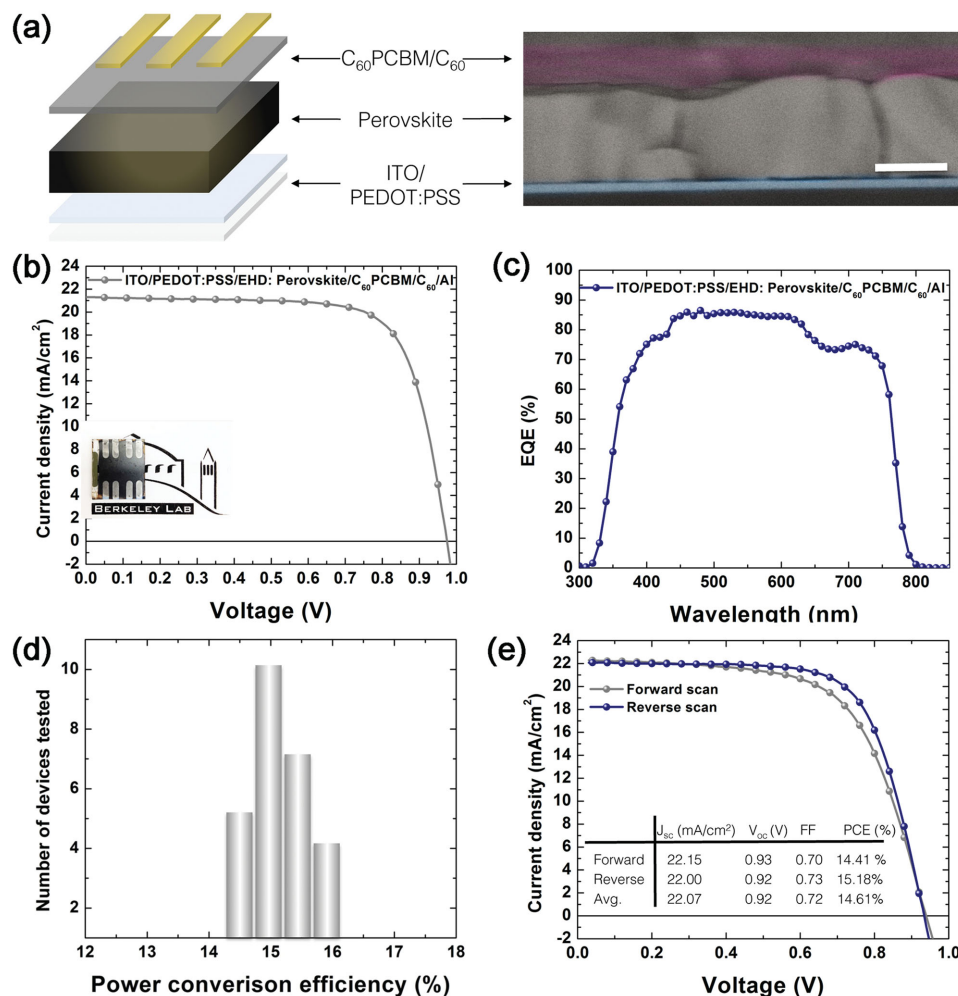


Figure 4. Device architecture and output characteristics of planar perovskite solar cells. a) Device architecture of the planar perovskite solar cell comprises of ITO/PEDOT:PSS/perovskite/C₆₀PCBM/C₆₀/Al. The false-colored, cross-sectional HRSEM image shows the well-defined interfaces between each layer. Scale bar is 500 nm. b) *I*-*V* curves and c) corresponding EQE are obtained and averaged from 20 devices. d) Histogram of photovoltaic efficiency for 26 devices shows the reproducibility and low variability of quality perovskite thin films produced by the CLIP process. e) *I*-*V* curves measured in forward (short circuit to open circuit) and reverse (open circuit to short circuit) directions with 10 mV voltage steps and 40 ms delay times under an AM 1.5G illumination. Inset shows the table of output characteristics, including forward, reverse scans, and the average of both, respectively.

after thermal annealing (Figure S6, Supporting Information). XRD, UV-vis and output *I*-*V* characteristics further confirm the preserved quality, integrity, and photovoltaic properties of perovskite active layers produced by the dual-sourced CLIP process (Figure S7 and Table S2, Supporting Information). With a wide variety of the organic/inorganic precursors, we envision that a wealthy suit of novel perovskites that combine complementary strengths from two different chemical worlds can be rationally and compositionally created, thus greatly enhancing the complexity and functionality.

The ability to create contiguous and crystalline grains also manifests in the steady output photovoltaic characteristics as a function of increasing thicknesses. It is known that grain size plays a pivotal role in efficient transport of dissociated charge carriers. In most sprayed coated perovskites, the thin film is largely limited to around 400 nm in order to match the in-plane dimension of grains. Consequently, the J_{sc} is significantly lower than that of thermal evaporation and solution process

counterparts due to the limited absorption profile. When thickness increases, the output *I*-*V* characteristics quickly deteriorate because of the defect-plagued transport pathways, particularly in the case of spray-coating approach where the multi-pass deposition is needed for achieving the desired thickness of perovskite absorbers. In contrast, high quality perovskite crystals with various thicknesses can be conveniently and continuously fabricated through simply increasing the flow rate, in a way similar to the additive manufacturing. For example, increasing the flow rate 26 $\mu\text{L min}^{-1}$ readily gives rise to the highest achievable thickness of 1130 nm. Detailed processing parameters with respect to various thin film thicknesses can be found in Scheme S3 (Supporting Information). Figure S8a (Supporting Information) features *I*-*V* curves as a function of increasing thicknesses of perovskite thin films (700 nm in black line, 950 nm in red line, and 1130 nm in green line). All three samples made of different thicknesses display comparable photoresponses, as PCE remains competitive over the full spectral

range (>11%). The decrease in J_{sc} may be attributed to the formation of uneven morphology as the peak-to-valley roughness surges to 80 nm when thin film thickness exceeds 900 nm. A similar trend is observed in the thickness dependent EQE measurement except for the region near the adsorption edges that flatten out as thickness increases (Figure S8b, Supporting Information). This can be attributed to the single path absorption of the thicker perovskite films. As previously shown in UV-vis spectra (Figure S3, Supporting Information), the single path adsorption near the onset of absorption edge became increasingly steep and gradually saturated when thin film thickness increases. Perovskite solar cells fabricated by CLIP process also demonstrated steady state measurements for J_{sc} is shown in Figure S9 (Supporting Information), which confirms the device performance parameters extracted from $I-V$ curves as well as demonstrating the reliability and reproducibility. These advantageous features with respect to the carrier transport again highlight the importance of preserving the integrity of perovskites during deposition. Further, $I-V$ curves obtained in reverse (from V_{oc} to J_{sc}) and forward directions (J_{sc} to V_{oc}) mesh well with the bulk crystalline nature of the perovskite thin films as summarized in Figure 4e. The overall PCEs of both reverse and forward directions are 15.18% and 14.41%, respectively, with an average of 14.79%. Note that the minor discrepancy in PCE mainly emanates from the FF of forward scan because the output characteristics such as V_{oc} and J_{sc} remain unchanged in

both directions. This is intriguing and deviates from most of the reports on the formation of large perovskite grains.

To further infer the discrepant nature of scan directions, we systematically explored the dynamics of photogenerated charge carriers at the interfaces and within perovskite layers. We first measured charge generation by means of photoluminescence (PL) and time-resolved photoluminescence lifetime measurements (TRPL) of thin film specimens made of $\text{CH}_3\text{NH}_3\text{PbI}_{3-x}\text{Cl}_x$, PEDOT:PSS/ $\text{CH}_3\text{NH}_3\text{PbI}_{3-x}\text{Cl}_x$, $\text{CH}_3\text{NH}_3\text{PbI}_{3-x}\text{Cl}_x/\text{C}_{60}\text{PCBM}$, and PEDOT:PSS/ $\text{CH}_3\text{NH}_3\text{PbI}_{3-x}\text{Cl}_x/\text{C}_{60}\text{PCBM}$ on ITO glass substrates, respectively. As featured in Figure 5a, the expected PL quenching occurs when the perovskite thin film (blue open circle) is in contact with either PEDOT:PSS (gray open circle) or C_{60}PCBM layers (olive open circle). The drastically reduced PL intensity suggests the effective extraction of charge carriers at both interfaces (red open circles). In parallel, TRPL also yields an average lifetime of ≈ 184 ns from neat perovskite thin film specimens (Figure 5b). This long lifetime can be translated to equivalently long carrier diffusion lengths that allow the use of thicker perovskite thin films for light harvesting. In particular, we observed a bimodal recombination process, an indication of large grains with good crystalline quality. PL lifetime significantly drops to 15 ns when the perovskite film is incorporated in full device architecture, originating from the rapid charge transfer at the interfaces. These spectral interpretations at macroscopic scale are in a good agreement with our output $I-V$

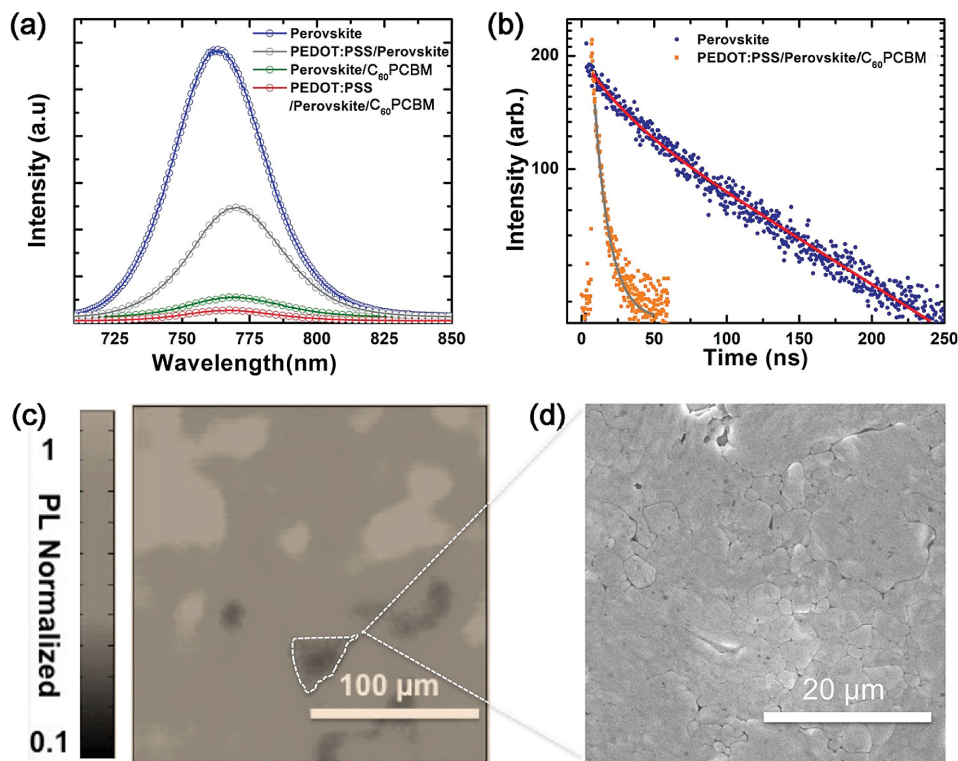


Figure 5. Spatially, spectrally, and temporally resolved photoluminescence spectroscopy. a) Photoluminescence of perovskite (blue), PEDOT:PSS/perovskite (gray), perovskite/ C_{60}PCBM (olive), and PEDOT:PSS/perovskite/ C_{60}PCBM (red) shows the effective quenching when paired with transport layers. b) Time-resolved photoluminescence lifetime of the perovskite thin film on the ITO glass and from the full device architecture. c) Photoluminescence mapping and d) corresponding SEM image on perovskite thin films spectrally interpret the spatial variation of crystalline grains over a large area ($200\ \mu\text{m} \times 200\ \mu\text{m}$ with $1\ \mu\text{m}$ resolution).

characteristics, thus ruling out the possibility of trap-assisted hysteresis within large area grains.

Since the integrity of grains in the out-of-plane directions remains largely intact, we thus surmise that the origin of variation between forward and reverse scan directions may arise from the hybrid crystalline morphology that consists of small grains tiled between spatially propagated perovskite networks. Previous studies have shown that PL intensity and lifetime varied across neighboring grains in the same film.^[30] Interfaces between these tightly packed grains showed a much weaker PL intensity as well as exhibiting a faster non-radiative decay. Due to the lateral dimensions of bulky perovskite grains that well extend into hundreds of micrometers, large area PL mapping (200 $\mu\text{m} \times 200 \mu\text{m}$, with 1 μm resolution) was employed to spectrally interpret the spatial uniformity within the thin film (Figure 5c). While the majority of PL mapping appears to be mostly uniform along the perovskite crystalline networks, the presence of the sporadically dispersed dark regions suggests the formation of local non-radiative pathways. Figure 5d presents the corresponding SEM image taken from the area of dimmer PL intensities, revealing a polygonal assembly of grains. This indicates that the smaller grains arranged in a polygon fashion may be responsible for the formation of defect states or shallow trapping levels. As a result, redistribution of charged carriers during forward and reverse scans is hampered by these localized recombination sites, therefore losing the momentum toward reaching equilibrium states. While ongoing research is currently carried out to explore the nature of the small mismatch of FF, one possible inroad to address this morphological inhomogeneity is the convergence of solvent assisted reactivation and vacuum assisted thermal annealing.^[30] For example, shallow traps arising from the grain boundaries can be effectively suppressed through the pyridine vapor assisted reduction process while the vacuum assisted thermal annealing vastly improves the overall crystallinity by the reconstruction of thin film morphology in tandem with stability in ambient conditions, thus concurrently improving the carrier dynamics and the fidelity of measurements.^[31] On the other hand, the implementation of vacuum assisted annealing should be directly compatible with in-line production, making it possible to realize a glass-in-perovskite-out inline production while preserving the competitive output characteristics.

4. Conclusion

In addition to the spectacular pace of efficiency improvement through the innovation of manufacturing routes, terrestrial deployment of perovskites is largely hindered by the fact that Pb has been a major constituent of all highly performing perovskite photovoltaics to date, raising environmentally hazardous concerns during processing, device fabrication, deployment, and disposal. While strenuous efforts have been dedicated to exploring alternatives of Pb, relatively little is investigated to efficiently manage Pb consumption during the deposition steps.^[32] Furthermore, to ensure both desired morphology and optimized coverage, excessive perovskite precursors are needed in the conventional spin-casting process. For example, nearly $\approx 100 \mu\text{L}$ of perovskite precursors (containing

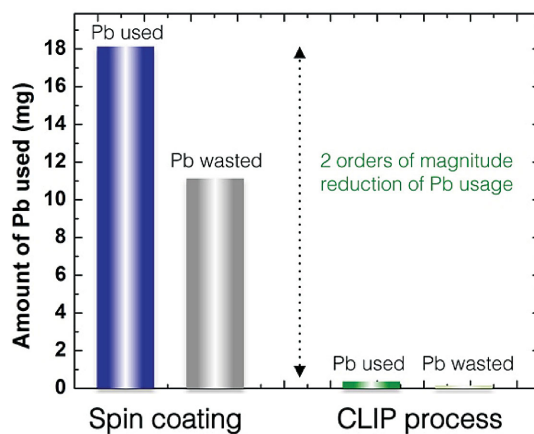


Figure 6. The consumption of Pb can be significantly reduced by two orders of magnitude when deposited for the same thickness of $\approx 500\text{--}525 \text{ nm}$, embodying an important step to meet the legislative regulations.

2.64 M MAI and 0.88 M PbCl_2) are typically used in each spin-casting cycle that accounts for $\approx 18.40 \text{ mg}$ of Pb usage; however, more than 70% of the solution was wasted emanating from the centrifugal forces in order to generate thin films with desired morphology over the entire substrates (typically set at 3000 rpm to deliver perovskite thin film thickness of $\approx 500 \text{ nm}$ over a $1.5 \text{ cm} \times 1.5 \text{ cm}$ substrate). The consumption of Pb will be further pushed into an exponential model when the scale of production becomes progressively close to an industrial standard, making it less competitive to the silicon based photovoltaics. In contrast, CLIP process requires only $1.70 \mu\text{L}$ of perovskite precursor solutions with same concentrations to generate a fully covered, continuous thin film with a comparable thickness of 525 nm (5 kV cm^{-1} , flow rate $18 \mu\text{L min}^{-1}$, and stage speed of 3.2 mm s^{-1}). Of paramount importance is the significant reduction of Pb during the fabrication process because over 90% of the precursor droplets are effectively used to constitute the active layers. This can be translated into that only $\approx 0.31 \text{ mg}$ of Pb in total will be needed in each spray cycle, a two orders of magnitude of reduction compared to that of spin-coating counterpart as summarized in **Figure 6**. The substantial reduction of Pb consumption during deposition thus diminishes the negative impact of Pb in large-scale production of perovskite-based photovoltaics, representing a significant step closer to meet the legislative regulations. Combined with the rapid development of moisture resistant passivation, high throughput production of highly stable perovskite photovoltaics with a combination of competitive PCE and limited environmental impact can be expected in the foreseeable future.^[10,18]

5. Experimental Section

Solar Cell Fabrication: MAI was prepared in accordance with the previously reported.^[33] Methylamine (CH_3NH_2) solution 33 wt% in absolute ethanol was reacted with hydroiodic acid (HI) 57 wt% in water with excess methylamine under nitrogen atmosphere in ethanol at room temperature. Typical quantities were 24 mL methylamine, 10 mL hydroiodic acid, and 100 mL ethanol. The resultant white powders of MAI were iteratively washed with diethyl ether and then dried at $60 \text{ }^\circ\text{C}$ in a vacuum oven for 24 h. MAI and PbCl_2 in a molar ratio of 3:1 were

stirred in a mixture of anhydrous DMSO and NMP (4:6, v/v) at 60 °C until no visibly distinguishable precipitation. Note that all the precursor solutions were prepared inside the glovebox and the final concentration was further diluted to 50 wt% before EHD spraying. PEDOT:PSS (Clevois, Al 4083) was spin-coated at 4000 rpm onto the ITO substrates pretreated with UV-ozone, followed by a thermal annealing at 120 °C for 20 min. Prior to EHD spraying, ITO/PEDOT:PSS substrates were again treated with UV-ozone for 40 s to remove organic contaminants as well as improving the wettability. Next, the $\text{CH}_3\text{NH}_3\text{PbI}_{3-x}\text{Cl}_x$ precursor solution was EHD sprayed. The distance between the spinneret tip (gauge 23 TW) and the ground (copper plate) was carefully kept at 2.5 cm. An external electric field of 12.5 kV was applied to ensure the generation of a multi-jet mode. The dynamics of EHD spraying were closely monitored through a high-speed camera (Phantom). The substrate temperature was kept at 35 °C to avoid the unwanted coffee ring effect. Flow rate was set at $18 \mu\text{L min}^{-1}$ while the moving speed of the linear motor stage (Newport, ILS 100LM) was programmed at 3.2 mm s^{-1} . Note that humidity of the fume hood was closely monitored to keep at below 20%. The resulting substrates were immediately transferred to a glass petri dish for 15 min prior to thermal annealing. Alternatively, spraying coating samples were made using the analogous conditions except for the pre-annealing of the substrate at 75 °C, emulating the spray-induced de-wetting process. All coating processes were completed inside the fume hood. Upon completion of EHD-cycles, perovskite thin films were immediately transferred into a petri dish to further initiate reorganization and optimization process. Finally, highly crystallized perovskite thin films were obtained through a hot air assisted annealing process (Heat gun, Master ProHeat 1100 Dualtemp) at 110 °C for 6 min. Specifically, the directional flow of hot air constantly creates turbulence at the air-perovskite liquid interfaces. Volatile MAI byproducts can thus be effectively removed through thermal annealing, thus leaving the room for rapid crystallization of perovskites. To ensure the surface uniformity, the distance between the heat gun and substrates was carefully kept at 21 cm. During the annealing process, samples were iteratively oscillated at a frequency of 5 mm s^{-1} . 20 mg mL^{-1} of C_{60} PCBM (Nano-C) was dissolved in dichlorobenzene solution and filtered before spin-coating onto the perovskite layer at 3000 rpm, followed by thermal annealing at 100 °C for an hour. To complete the photovoltaic cell, 30 nm of C_{60} and 70 nm of Al were thermally evaporated through a shadow mask. The device area was determined to be $\approx 0.13 \text{ cm}^2$. I-V characteristics of photovoltaic cells were taken using a Keithley 2400 source measurement unit under a simulated AM1.5G spectrum. Light intensity was calibrated by a KG-5 silicon diode. EQE spectra were taken using a QE-5 measurement system (Enli Tech., Taiwan).

Characterizations: The morphological and topological information of CLIP generated perovskite thin films were obtained using a combination of FESEM (Zeiss, ULTRA-55) integrated with an energy dispersive X-ray spectroscopy, AFM (Multimode, DI), and optical microscopy (Leica, DM-2500). Thickness of perovskite thin films was determined through cross-sectional SEM images. The XRD characterizations were collected using a Bruker AXS D8 Discover GADDS X-ray diffractometer (Cu K α radiation, $\lambda = 1.54059 \text{ \AA}$). A pulsed supercontinuum source (NTK Photonics) at 690 nm wavelength with 1.2 mW cm^{-2} power was used for optical measurements. The PL measurements were done using an Action 150i spectrometer, which disperses the signal onto a thermoelectrically cooled CCD. For time-resolved PL measurement, a 690 nm pulsed light source was used at a Rep rate of 3.9 MHz.

Supporting Information

Supporting Information is available from the Wiley Online Library or from the author.

Acknowledgements

V.T. gratefully acknowledges the support of user proposal (#3192 and #3715) at the Molecular Foundry, Lawrence Berkeley National

Lab, supported by the Office of Basic Energy Sciences, of the U.S. Department of Energy under Contract No. DE-AC02-05CH11231. S.G. would like to acknowledge the National Science Foundation DMR-1056860. The authors are indebted to Daniel Sun and Wendy L. Quen for XRD characterizations, Dr. Yi Liu and Teresa L. Chen for the fruitful discussion in charge carrier dynamics, and Marisol Prado and Jose Hernandez for the assistance in instrumentation.

Received: November 25, 2015

Revised: January 26, 2016

Published online: February 22, 2016

- [1] M. A. Green, A. Ho-Baillie, H. J. Snaith, *Nat. Photonics* **2014**, *8*, 506.
- [2] K. N. Liang, D. B. Mitzi, M. T. Prikas, *Chem. Mater.* **1998**, *10*, 403.
- [3] Q. Chen, H. P. Zhou, Z. R. Hong, S. Luo, H. S. Duan, H. H. Wang, Y. S. Liu, G. Li, Y. Yang, *J. Am. Chem. Soc.* **2014**, *136*, 622.
- [4] H. S. Kim, I. Mora-Sero, V. Gonzalez-Pedro, F. Fabregat-Santiago, E. J. Juarez-Perez, N. G. Park, J. Bisquert, *Nat. Commun.* **2013**, *4*, 2242.
- [5] S. Y. Sun, T. Salim, N. Mathews, M. Duchamp, C. Boothroyd, G. C. Xing, T. C. Sum, Y. M. Lam, *Energy Environ. Sci.* **2014**, *7*, 399.
- [6] S. D. Stranks, G. E. Eperon, G. Grancini, C. Menelaou, M. J. P. Alcocer, T. Leijtens, L. M. Herz, A. Petrozza, H. J. Snaith, *Science* **2013**, *342*, 341.
- [7] H. P. Zhou, Q. Chen, G. Li, S. Luo, T. B. Song, H. S. Duan, Z. R. Hong, J. B. You, Y. S. Liu, Y. Yang, *Science* **2014**, *345*, 542.
- [8] N. J. Jeon, J. H. Noh, W. S. Yang, Y. C. Kim, S. Ryu, J. Seo, S. I. Seok, *Nature* **2015**, *517*, 476.
- [9] a) Z. K. Tan, R. S. Moghaddam, M. L. Lai, P. Docampo, R. Higler, F. Deschler, M. Price, A. Sadhanala, L. M. Pazos, D. Credgington, F. Hanusch, T. Bein, H. J. Snaith, R. H. Friend, *Nat. Nanotechnol.* **2014**, *9*, 687; b) K. Tvingstedt, O. Malinkiewicz, A. Baumann, C. Deibel, H. J. Snaith, V. Dyakonov, H. J. Bolink, *Sci. Rep.* **2014**, *4*, 6071; c) H. Snaith, L. Schmidt-Mende, *APL Mater.* **2014**, *2*, 8; d) T. Leijtens, S. D. Stranks, G. E. Eperon, R. Lindblad, E. M. J. Johansson, I. J. McPherson, H. Rensmo, J. M. Ball, M. M. Lee, H. J. Snaith, *ACS Nano* **2014**, *8*, 7147; e) J. T. W. Wang, J. M. Ball, E. M. Barea, A. Abate, J. A. Alexander-Webber, J. Huang, M. Saliba, I. Mora-Sero, J. Bisquert, H. J. Snaith, R. J. Nicholas, *Nano Lett.* **2014**, *14*, 724; f) T. Leijtens, G. E. Eperon, S. Pathak, A. Abate, M. M. Lee, H. J. Snaith, *Nat. Commun.* **2013**, *4*, 2885; g) P. Docampo, J. M. Ball, M. Darwich, G. E. Eperon, H. J. Snaith, *Nat. Commun.* **2013**, *4*, 2761; h) M. Z. Liu, M. B. Johnston, H. J. Snaith, *Nature* **2013**, *501*, 395; i) J. M. Ball, M. M. Lee, A. Hey, H. J. Snaith, *Energy Environ. Sci.* **2013**, *6*, 1739.
- [10] M. D. McGehee, *Nature* **2013**, *501*, 323.
- [11] a) B. Conings, L. Baeten, C. De Dobbelaere, J. D'Haen, J. Manca, H. G. Boyen, *Adv. Mater.* **2014**, *26*, 2041; b) A. Dualeh, N. Tetreault, T. Moehl, P. Gao, M. K. Nazeeruddin, M. Gratzel, *Adv. Funct. Mater.* **2014**, *24*, 3250.
- [12] J. Burschka, N. Pellet, S. J. Moon, R. Humphry-Baker, P. Gao, M. K. Nazeeruddin, M. Gratzel, *Nature* **2013**, *499*, 316.
- [13] Q. Wang, Y. C. Shao, Q. F. Dong, Z. G. Xiao, Y. B. Yuan, J. S. Huang, *Energy Environ. Sci.* **2014**, *7*, 2359.
- [14] N. J. Jeon, J. H. Noh, Y. C. Kim, W. S. Yang, S. Ryu, S. I. Seol, *Nat. Mater.* **2014**, *13*, 897.
- [15] Y. H. Deng, E. Peng, Y. C. Shao, Z. G. Xiao, Q. F. Dong, J. S. Huang, *Energy Environ. Sci.* **2015**, *8*, 1544.
- [16] W. Y. Nie, H. H. Tsai, R. Asadpour, J. C. Blancon, A. J. Neukirch, G. Gupta, J. J. Crochet, M. Chhowalla, S. Tretiak, M. A. Alam, H. L. Wang, A. D. Mohite, *Science* **2015**, *347*, 522.

- [17] L. M. Chen, Z. R. Hong, W. L. Kwan, C. H. Lu, Y. F. Lai, B. Lei, C. P. Liu, Y. Yang, *ACS Nano* **2010**, *4*, 4744.
- [18] A. Y. Mei, X. Li, L. F. Liu, Z. L. Ku, T. F. Liu, Y. G. Rong, M. Xu, M. Hu, J. Z. Chen, Y. Yang, M. Gratzel, H. W. Han, *Science* **2014**, *345*, 295.
- [19] A. T. Barrows, A. J. Pearson, C. K. Kwak, A. D. F. Dunbar, A. R. Buckley, D. G. Lidzey, *Energy Environ. Sci.* **2014**, *7*, 2944.
- [20] a) R. D. Deegan, O. Bakajin, T. F. Dupont, G. Huber, S. R. Nagel, T. A. Witten, *Nature* **1997**, *389*, 827; b) J. X. Huang, F. Kim, A. R. Tao, S. Connor, P. D. Yang, *Nat. Mater.* **2005**, *4*, 896.
- [21] Z. G. Xiao, C. Bi, Y. C. Shao, Q. F. Dong, Q. Wang, Y. B. Yuan, C. G. Wang, Y. L. Gao, J. S. Huang, *Energy Environ. Sci.* **2014**, *7*, 2619.
- [22] a) D. Kim, A. L. Giermann, C. V. Thompson, *Appl. Phys. Lett.* **2009**, *95*, 251903; b) J. P. Ye, C. V. Thompson, *Appl. Phys. Lett.* **2010**, *97*; c) C. V. Thompson, *Annu. Rev. Mater. Res.* **2012**, *42*, 399; d) G. H. Kim, R. V. Zucker, J. Ye, W. C. Carter, C. V. Thompson, *J. Appl. Phys.* **2013**, *113*, 043512; e) O. Kovalenko, J. R. Greer, E. Rabkin, *Acta Mater.* **2013**, *61*, 3148; f) A. Kosinova, L. Klinger, O. Kovalenko, E. Rabkin, *Scr. Mater.* **2014**, *82*, 33; g) J. Ye, *Appl. Phys. Express* **2014**, *7*, 085601.
- [23] A. L. Yarin, D. A. Weiss, *J. Fluid Mech.* **1995**, *283*, 141.
- [24] A. Jaworek, A. T. Sobczyk, *J. Electrostat.* **2008**, *66*, 197.
- [25] J. M. D'arcy, H. D. Tran, V. C. Tung, A. K. Tucker-Schwartz, R. P. Wong, Y. Yang, R. B. Kaner, *Proc. Natl. Acad. Sci. USA* **2010**, *107*, 19673.
- [26] M. Kaltenbrunner, G. Adam, E. D. Glowacki, M. Drack, R. Schwodiauer, L. Leonat, D. H. Apaydin, H. Groiss, M. C. Scharber, M. S. White, N. S. Sariciftci, S. Bauer, *Nat. Mater.* **2015**, *14*, 1032.
- [27] G. Li, V. Shrotriya, J. S. Huang, Y. Yao, T. Moriarty, K. Emery, Y. Yang, *Nat. Mater.* **2005**, *4*, 864.
- [28] a) E. Mansfield, E. E. Ross, G. D. D'Ambruso, J. P. Keogh, Y. Huang, C. A. Aspinwall, *Langmuir* **2007**, *23*, 11326; b) X. Fanton, A. M. Cazabat, *Langmuir* **1998**, *14*, 2554; c) C. Girotto, D. Moia, B. P. Rand, P. Heremans, *Adv. Funct. Mater.* **2011**, *21*, 64.
- [29] a) Q. Chen, H. P. Zhou, Y. H. Fang, A. Z. Stieg, T. B. Song, H. H. Wang, X. B. Xu, Y. S. Liu, S. R. Lu, J. B. You, P. Y. Sun, J. McKay, M. S. Goorsky, Y. Yang, *Nat. Commun.* **2015**, *6*, 7269; b) Y. Tidhar, E. Edri, H. Weissman, D. Zohar, G. Hodes, D. Cahen, B. Rybtchinski, S. Kirmayer, *J. Am. Chem. Soc.* **2014**, *136*, 13249; c) S. T. Williams, F. Zuo, C. C. Chueh, C. Y. Liao, P. W. Liang, A. K. Y. Jen, *ACS Nano* **2014**, *8*, 10640.
- [30] D. W. deQuilettes, S. M. Vorpahl, S. D. Stranks, H. Nagaoka, G. E. Eperon, M. E. Ziffer, H. J. Snaith, D. S. Ginger, *Science* **2015**, *348*, 683.
- [31] F. X. Xie, D. Zhang, H. M. Su, X. G. Ren, K. S. Wong, M. Gratzel, W. C. H. Choy, *ACS Nano* **2015**, *9*, 639.
- [32] F. Hao, C. C. Stoumpos, D. H. Cao, R. P. H. Chang, M. G. Kanatzidis, *Nat. Photonics* **2014**, *8*, 489.
- [33] M. M. Lee, J. Teuscher, T. Miyasaka, T. N. Murakami, H. J. Snaith, *Science* **2012**, *338*, 643.